Huang diffuse scattering from dislocation loops and cobalt precipitates in copper*

Bennett C. Larson and W. Schmatz†
Solid State Division, Oak Ridge National Laboratory, Oak Ridge, Tennessee 37830
(Received 26 December 1973)

High-resolution measurements of the Huang diffuse scattering from dislocation loops in neutron-irradiated copper and cobalt precipitates in Cu:1-wt%-Co crystals have been carried out close to the (200) and (111) reflections using a three-axis x-ray diffractometer. These measurements have been compiled in the form of diffuse intensity contours and compared with calculations based on the dipole-force model for dislocation loops and spherical precipitates. Good agreement was found between the measured and calculated contours and it was shown that the symmetry of the defects could be determined from these measurements. The necessity of considering the elastic anisotropy of the lattice in the calculations was also demonstrated.

INTRODUCTION

Recent theoretical work[1-4] has shown that rather detailed information on lattice defects can be obtained from diffuse scattering near reciprocal-lattice points (Huang scattering). By relating the Huang scattering to the dipole-force tensor of the defects, information on the symmetry, size, and concentration of the defects can be realized.

Several experimental studies have already been carried out using this approach to study self-interstitials in aluminum,[5] copper,[6] and potassium bromide,[7] as well as oxygen interstitials in niobium.[8] Aggregation of these point defects into clusters was also observed. In these studies the scattering along a few appropriate directions in reciprocal space was measured using focusing geometries in order to obtain sufficient scattering intensities from the point defects.

In the present study the Huang scattering from dislocation loops and spherical precipitates in copper has been investigated using a three-axis diffractometer in order that measurements could be carried out close to the reciprocal-lattice points as required for defects of extended sizes. Measurements were made throughout areas close to the (111) and (200) reflections and these data were used to construct isointensity contours demonstrating the general features of the Huang scattering expected for these defects. These features include the influence of lattice anisotropy, the shape of the symmetric and antisymmetric scattering contours for the two types of defect aggregates, and the sign of the antisymmetric scattering, which is related to the sign of the dilatation of the lattice caused by the defects.

THEORY

The theoretical framework required for this study can be acquired largely from previous work on Huang scattering[1-4,9-12] and only the results pertinent to this study, the relationship between the dipole-force tensor and the distribution of the diffuse scattering around the reciprocal-lattice points, will be covered in detail.

The x-ray power scattered into an element of solid angle $(\Delta\Omega)_D$, centered at a point $\vec{q}$ relative to the reciprocal-lattice vector $\vec{h}$, by N_d defect centers with scattering cross section $d\sigma_h(\vec{q})/d\Omega$, is given by

$$I_h(\vec{q}) = N_d I_0 \frac{d\sigma_h(\vec{q})}{d\Omega} (\Delta\Omega)_D , \tag{1}$$

where I_0 is the power in the incident beam. $d\sigma_h(\vec{q})/d\Omega$ represents the weighted average of all the momentum transfers $\vec{q}$ contributing to the scattering in the solid angle $(\Delta\Omega)_D$. The scattering cross section per defect can be written

$$\frac{d\sigma_h(\vec{q})}{d\Omega} = (r_e f_a)^2 \, |A_h(\vec{q})|^2 , \tag{2}$$

where r_e is the classical electron radius and f_a is the atomic scattering factor including thermal and polarization effects. $A_h(\vec{q})$ is the scattering amplitude. For the relatively large defect clusters of interest here $|A_h(\vec{q})|^2$ can be approximated for $qR < 1$ (R = cluster radius) by[1,9]

$$|A_h(\vec{q})|^2 \simeq [\,|\vec{h}\cdot\vec{s}(\vec{q})|^2 - 2i\vec{h}\cdot\vec{s}(\vec{q}) L_h(\vec{q})]\, e^{-2L_h(\vec{q})} , \tag{3}$$

where $\vec{s}(\vec{q})$ is the Fourier transform of the antisymmetric displacement field, $\vec{s}(\vec{r})$, of the defects, and $L_h(\vec{q})$ is the static Debye parameter[13] for the defects. Since $\vec{s}(\vec{q})$ is antisymmetric [$\vec{s}(\vec{q}) = -\vec{s}(-\vec{q})$], the first term in Eq. (3) is symmetric and the second term is antisymmetric.

The symmetric term, given in terms of the Fourier-transformed elastic Green's function G_{in} and the dipole-force tensor P_{nm}, is given by[9]

$$|\vec{h}\cdot\vec{s}(\vec{q})|^2 = |(h_i/V_c)G_{in}P_{nm}q_m|^2 . \quad (4)$$

Summation over repeated indices is assumed and

$$G_{in}=\frac{1}{q^2}\left\{\frac{\delta_{in}}{C_{44}+de_n^2}-\frac{e_ie_n}{(C_{44}+de_i^2)(C_{44}+de_n^2)}\right.$$
$$\left.\times(C_{44}+C_{12})\right/\left[1+\sum_k\left(\frac{C_{44}+C_{12}}{C_{44}+de_k^2}\right)e_k^2\right] , \quad (5)$$

where $e_i=q_i/|\vec{q}|$, $d=C_{11}-C_{12}-2C_{44}$, and the C's are the elastic constants. The dipole-force tensor of a spherical defect cluster is isotropic[4] and is given in terms of the strength P_0 of the cluster by

$$P_{nm}=P_0\delta_{nm} . \quad (6)$$

For dislocation loops[3] the force tensor is

$$P_{nm}=(C_{12}\,\mathrm{Tr}\Omega_{nm}+d\Omega_{nn})\delta_{nm}+2C_{44}\Omega_{nm} , \quad (7)$$

where [not to be confused with $(\Delta\Omega)_D$ in Eq. (1)]

$$\Omega_{nm}=\tfrac{1}{2}(F_nb_m+F_mb_n) , \quad (8)$$

in which $\vec{b}$ is the Burgers vector of the loop and $\vec{F}$ is the area of the loop with direction normal to the loop plane. The symmetric scattering given by Eq. (4) contains the information on the symmetry of the defect as characterized by the dipole-force tensor. However, since all cubic-equivalent permutations of defect orientations must be considered equally populated with defects, Eq. (4) must be averaged over all these orientations. This has been carried out for the general case with the result that[3,4]

$$\langle|\vec{h}\cdot\vec{s}(\vec{q})|^2\rangle=\left(\frac{h}{q}\right)^2\sum_{i=1}^{3}\gamma_i\pi_i , \quad (9)$$

where $\langle\ \rangle$ denotes the average over cubic-equivalent orientations and

$$\gamma_1=\tfrac{1}{3}(\mathrm{Tr}\,T_{ij})^2 ,$$
$$\gamma_2=\frac{1}{3}\sum_{i>j}(T_{ii}-T_{jj})^2 , \quad (10)$$
$$\gamma_3=\frac{1}{2}\sum_{i>j}(T_{ij}+T_{ji})^2 ,$$

and where

$$T_{ij}=(\hat{h}_k/V_c)g_{ki}e_j \quad (11)$$

with $\hat{h}_k=h_k/|\vec{h}|$ and $g_{ki}=q^2G_{ki}$. Similarly,

$$\pi_1=\tfrac{1}{3}(\mathrm{Tr}\,P_{nm})^2 ,$$
$$\pi_2=\frac{1}{6}\sum_{n>m}(P_{nn}-P_{mm})^2 , \quad (12)$$
$$\pi_3=\frac{2}{3}\sum_{n>m}P_{nm}^2 ,$$

where any of the cubic equivalent permutations of P_{nm} can be used to calculate the π's in this equation. Of course, this average is trivial for the case of a spherical defect cluster which has no preferred direction.

The antisymmetric term in Eq. (3) introduces an asymmetry into the scattering, and since $L_h(\vec{q})$ is always positive for small q's, the sign of this term is determined by $-i\vec{h}\cdot\vec{s}(\vec{q})$, which for $\vec{q}\cdot\vec{h}>0$ is real and positive for defects causing positive dilatation of the lattice (i.e., interstitials) and negative for defects contracting the lattice. The magnitude of $L_h(\vec{q})$ must be calculated by a numerical integration in general,[9] but for small q values it is constant and a reasonable estimate of its magnitude can be obtained from the approximate relationships for the isotropic case. These are[4]

$$L_h(\vec{q})=\frac{\sqrt{2}}{15V_c}\left|\frac{hP_0}{C_{11}}\right|^{3/2} \quad (13)$$

for clusters, and similarly for loops averaged over all orientations

$$L_h(\vec{q})=R^3|hb|^{3/2}/2V_c , \quad (14)$$

where R is the radius. Assuming $L_h(\vec{q})$ is given sufficiently well by Eqs. (13) and (14), the average of the antisymmetric term analogous to Eq. (9) requires simply an average of $i\vec{h}\cdot\vec{s}(\vec{q})$. Since the off-diagonal elements of P_{nm} average to zero and the diagonal elements average to $\frac{1}{3}\mathrm{Tr}\,P_{nm}$ in this process, the antisymmetric contours must have the same form for all P_{nm}. The form is that expected for spherical defects ($P_{nm}=P_0\delta_{nm}$) and, in particular,

$$\langle i\vec{h}\cdot\vec{s}(\vec{q})\rangle=(h/q)(\pi_1\gamma_1)^{1/2} . \quad (15)$$

From this it can be seen that when $L_h(\vec{q})$ is constant, the isointensity contours near the reciprocal-lattice points are given by $|\vec{q}|\propto(\pi_1\gamma_1)^{1/2}$, where γ_1 is a function of $\vec{q}$. This is the same form as the symmetric intensity in Eq. (9) for defects with an isotropic dipole-force tensor ($\pi_2=\pi_3=0$, e.g., spherical precipitates).

Equations (9) and (15) can be used to calculate the scattering cross sections and intensity distributions for the small q region ($qR\ll1$) and should give reasonable results out to $qR\sim1$.[9] The general features of these cross sections have been discussed in detail previously[1-4,9-12] and they will only be recalled here. (i) The symmetric cross section is proportional to $(h/q)^2$. (ii) The antisymmetric cross section is proportional to $h^{5/2}/q$. (iii) For $\vec{q}\parallel\vec{h}$, the antisymmetric cross section is >0 for defects expanding the lattice (i.e., interstitials). (iv) Conversely, for $\vec{q}\parallel\vec{h}$, the antisymmetric cross section is <0 for defects contracting the lattice (vacancies). (v) The symmetric term contains the information on the symmetry of the defect and is related to the long-range part of the displacement field of the defects. (vi) The antisymmetric term

carries no first-order information on the symmetry of the defects, but through $L_h(\vec{q})$ does contain information on the highly distorted region close to the defect.

EXPERIMENTAL

The diffuse scattering measurements were made using a three-axis diffractometer as shown in Fig. 1. Making use of nondispersive geometry and low-dislocation density crystals, the analyzer crystal acts as a collimator for the scattered x rays accepting only those x rays that strike it within the width of the Bragg reflection. In the plane of diffraction (defined by $\vec{k}_0$ and $\vec{h}$ in this case) this leads to a resolution of $\Delta q \simeq hW$, where W is the intrinsic width of the Bragg reflection. Since the "integrated intensity" of the Bragg reflection is numerically equal to the effective angular range with reflectivity 1, replacing W above by the "integrated intensity" of the Bragg reflection of the analyzer gives directly the effective acceptance window, Δq, measured along the Ewald sphere. This is $\sim \pm 2\times10^{-4}$ Å^{-1} for low-order reflections in copper using Cu$K\alpha$ radiation. The resolution out of the plane of diffraction (i.e., vertical divergence) was limited by the use of a slit system which resulted in a divergence that was considerably greater than that in the plane of diffraction. The geometry was composed of an x-ray source (0.4mm), a 0.4-mm slit preceding the sample, and a 0.4-mm slit at the detector with about 300 mm between each of these components. This corresponds to a root-mean-square deviation $\Delta q \approx \pm 4\times10^{-3}$ Å^{-1} out of the plane of diffraction. This vertical divergence does not seriously affect the effective $\vec{q}$ value for $q \gtrsim 7\times10^{-3}$ Å^{-1} and in cases where equal intensity contours are normal to $\vec{q}$ (which holds if the plane of diffraction is a mirror plane) the effect on the measured intensities is further minimized.

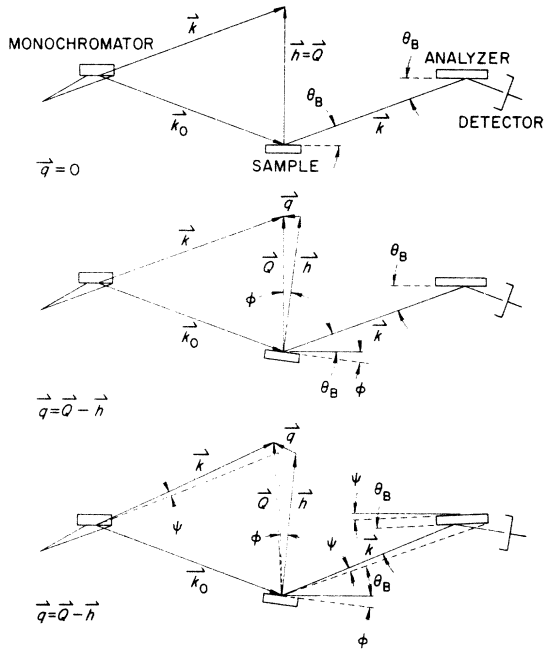

FIG. 1. Geometry of the diffuse scattering measurement using a three-axis diffractometer.

Considering the geometry in Fig. 1, monochromatic x rays, $\vec{k}_0$, incident on the sample, are scattered to a point $\vec{h}+\vec{q}=\vec{Q}$ (required by energy conservation to be on the Ewald sphere) and those scattered rays $\vec{k}$ striking the analyzer at the Bragg angle θ_B are reflected into the detector. Keeping the analyzer fixed and rotating the sample a small angle ϕ off the Bragg position, the diffuse intensity at $q=h\phi$ (in a direction perpendicular to $\vec{h}$) is measured by the detector as shown in the middle illustration. Rotating the analyzer an angle ψ, as depicted in the bottom configuration, an additional component $k\psi$ along the Ewald sphere is added to $\vec{q}$. $\vec{q}$ can therefore be resolved into $k\psi\cos\theta_B$ parallel to $\vec{h}$ and $h\phi + k\psi\sin\theta_B$ perpendicular to $\vec{h}$.

The procedure in this experiment was to set the analyzer angle ψ and record the diffuse scattering as a function of ϕ. These scans were carried out such that the scattered intensity was recorded for increments of $h\Delta\phi \sim 10^{-3}$ Å^{-1} and $k\Delta\psi \sim 1$–2×10^{-3} Å^{-1} depending on the density of points required to determine the intensity contours.

Scattering from the wings of the Bragg reflections, thermal diffuse scattering and other background scattering not related to the defects being studied were removed by subtracting the scattering from an unirradiated (or unprecipitated Cu:1-wt%-Co) copper crystal. The general background level was extremely low, as expected,[14] except along the three very narrow traces corresponging to the scattering from the wings of the Bragg reflection of the monochromator, sample, and analyzer, respectively. The observed characteristics of these traces seemed to be in accord with the dynamical diffraction theory and they will not be dealt with in detail here.

The samples used in these measurements were those used in previous experiments. One of the samples was irradiated to a dose of 10.8×10^{18} n/cm^2 ($E>0.6$ MeV) at 43 °C and has been extensively studied by anomalous transmission,[15] integral diffuse scattering[16] and lattice parameter measurements.[17] From these experiments, as well as associated electron-microscopy work, the defects present in this sample were known to be predominantly small dislocation loops. The Cu:1-wt%-Co precipitated sample had recently been the subject of a detailed investigation by x-ray topog-

raphy, Huang diffuse scattering, and lattice-parameter changes, as well as small-angle scattering by neutrons.[18] In addition, this system has been extensively studied by electron microscopy[19] so that in general it could be inferred that this sample, aged at 570 °C for 17 h, contained nearly spherical cobalt precipitates in the size range of 50–100-Å radius.

Aside from the small clustered defects (and possibly unclustered point defects not affecting this study), these crystals were considered essentially perfect from the standpoint of dynamical diffraction as their Bragg-reflection profiles gave essentially the intrinsic widths and therefore measurements close to the reciprocal-lattice points were no problem. The Cu:1-wt%-Co crystal was actually composed of cells ~1×1×10 mm which were slightly misoriented with respect to neighboring cells, but the x-ray beam was small enough that measurements could be made within one cell, inside of which there were no orientation changes, and the Bragg widths were those expected for a perfect copper crystal.

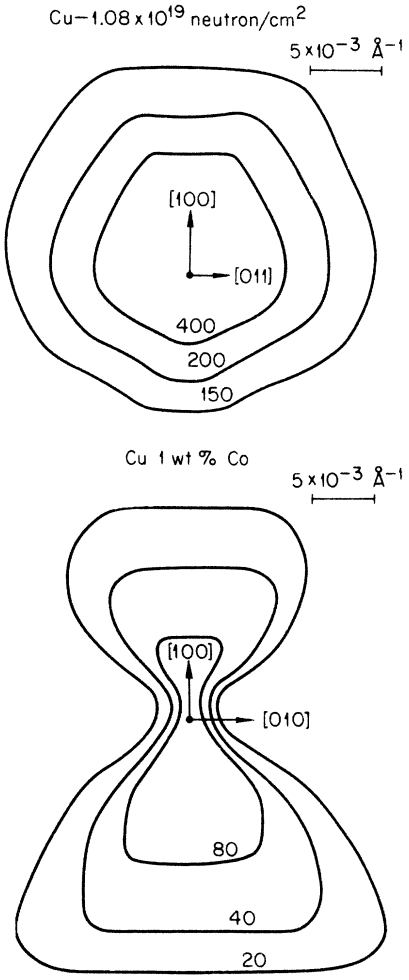

FIG. 2. Measured diffuse scattering contours near the (200) reflection from neutron-irradiated copper and Cu:1-wt%-Co.

RESULTS

The Huang diffuse scattering measurements made near the (200) and (111) reflections are presented in the form of intensity contours in Figs. 2 and 3 for both the neutron-irradiated and cobalt-precipitated samples. For $\vec{h} = (2, 0, 0)$, the scattering from the irradiation crystal (containing dislocation loops) has a characteristically different shape from that of the precipitated samples (containing spherical precipitates). In addition, the scattering is considerably asymmetric with the sense of the asymmetry such that there is more intensity for $\vec{q}\cdot\vec{h} > 0$ from the loops and there is more intensity for $\vec{q}\cdot\vec{h} < 0$ from the spherical precipitates. These asymmetries are as expected from Eq. (15) since the interstitial loops, which expand the lattice, are responsible for most of the scattering in the irradiated sample as a result of having larger average sizes than the vacancy loops, and since cobalt precipitates are known to contract the copper lattice. The contours around the (111) reflections in Fig. 3 demonstrate the same asymmetry prop-

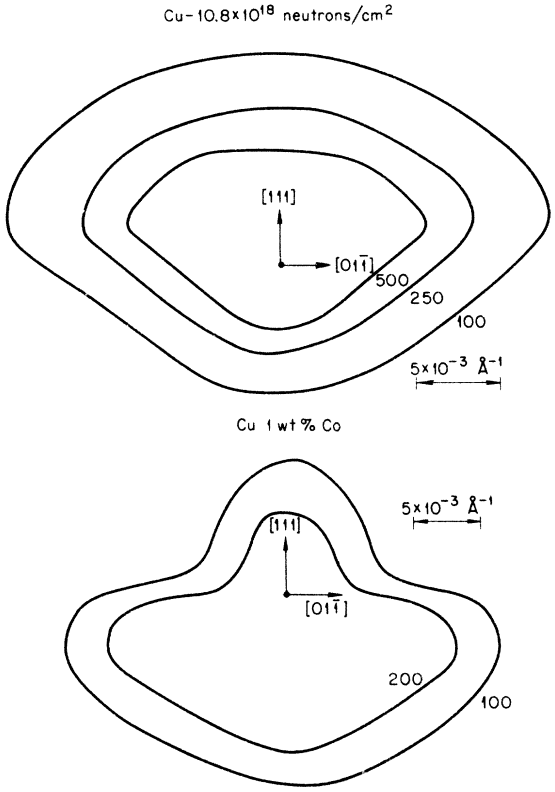

FIG. 3. Measured diffuse scattering contours near the (111) reflection for neutron-irradiated copper and Cu: 1-wt%-Co.

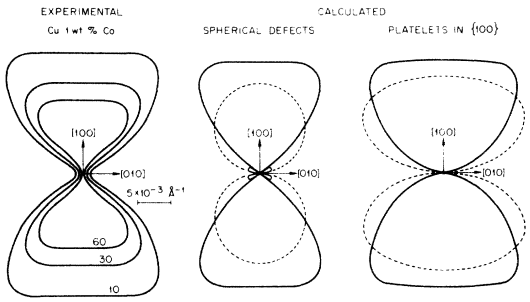

FIG. 4. Symmetrical part of the diffuse scattering near the (200) reflection from Cu: 1-wt%-Co. The calculated curves represent diffuse scattering contours for spherical clusters and platelets on {100} planes, assuming elastic isotropy (dashed) and elastic anisotropy (solid) in the copper lattice.

erties seen in the (200) case, although the shape of the observed contours for the two types of defects is not as strikingly different.

The intensities in Figs. 2 and 3 have been decomposed into symmetric and antisymmetric parts as suggested by Eq. (3) and the symmetric parts of these experimentally observed intensities are plotted in Figs. 4–7 along with calculated contours for various defect models. The experimental curves were generated by taking $\frac{1}{2}[I(\vec{q})+I(-\vec{q})]$ (where $\vec{q}$ is positive or negative, depending on whether $\vec{q}\cdot\vec{h}$ is positive or negative) and plotting the average of symmetry related points. This tended to smooth spurious wiggles in the contours and results in contours that have the full symmetry even though the raw intensity contours (see Figs. 2 and 3) show some experimental deviations. The calculated contours were obtained using Eqs. (9), (15), and $C_{11}=16.84$, $C_{12}=12.14$, and $C_{44}=7.54$ $\times 10^{-11}$ dyn/cm^2 as the elastic constants for copper. The isotropic average results were obtained using $\overline{C}_{12}=C_{12}+\frac{1}{5}d$, $\overline{C}_{44}=C_{44}+\frac{1}{5}d$, and $\overline{C}_{11}=\overline{C}_{12}+2\overline{C}_{44}$ and are denoted by the dashed curves in the figures.

The symmetric scattering near the (200) reflection resulting from the cobalt precipitates is shown in Fig. 4 where it can be seen that there is essentially no intensity perpendicular to $\vec{h}$, characteristic of spherical defects. The calculated contours for platelets on the {100} planes as well as those for spherical defects are also shown in this figure. Neither of the models approximates the measured scattering contours using the isotropic average elastic constants (dashed curves); however, the calculations considering the anisotropy indicate that either of these two models could adequately represent the measured data. Since the little "rabbit ears" in the center of the contours for the spherical defects would not be resolvable in this experiment, this reflection does not offer the possibility of distinquishing between {100} platelets and spheres; however, platelets on {111} or {110} planes could be ruled out as they would produce contours similar to those in Fig. 6. The symmetrical intensity around the (111) reflection shown in Fig. 5 makes a clear distinction between {100} platelets and spherical defects in favor of the spheres, as was to be expected. Small deviations from sphericity would of course not be detected.

The symmetric intensity contours near the (200) reflection from the irradiated crystal (containing dislocation loops) are shown in Fig. 6. While these contours are in qualitative agreement with the calculations for loops on {111} or {110} planes, they tend to favor the {111} orientation, although there seems to be somewhat more intensity perpendicular to $\vec{h}$ than predicted by either of these models ($b=\langle 111\rangle$, $A=\{111\}$ produces contours intermediate of the two illustrated). There is no trouble in distinguishing these contours from those in Fig. 4, representative of spheres or {100} platelets. Figure 7 shows the measured and calculated contours around the (111) reflection and there is in this case a close resemblance of the measured contours with both of the calculated contour shapes. This reflection offers little possibility of distinguishing between these particular habit planes and Burgers vectors and it is also not ideal for distinguishing between loops and spheres because these contours

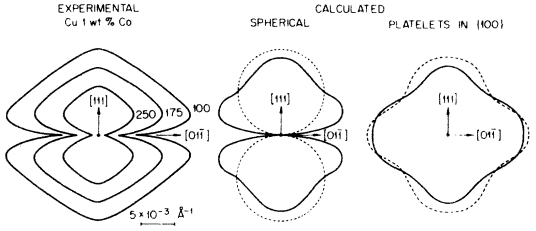

FIG. 5. Symmetrical part of the diffuse scattering near the (111) reflection from Cu: 1-wt%-Co. The calculations are for spherical clusters and platelets on {100} planes assuming elastic isotropy (dashed) and anisotropy (solid) in the copper lattice.

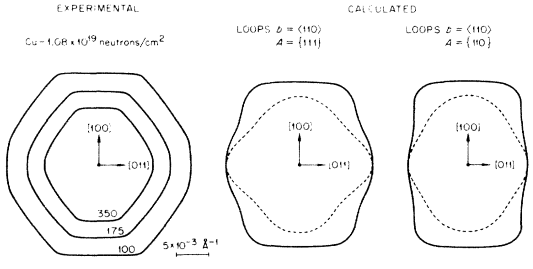

FIG. 6. Symmetrical part of the diffuse scattering near the (200) reflection from neutron-irradiated copper. The calculations represent the scattering from loops with Burgers vectors $b=\langle 110\rangle$ on {111} and {110} planes assuming elastic isotropy (dashed) and anisotropy (solid).

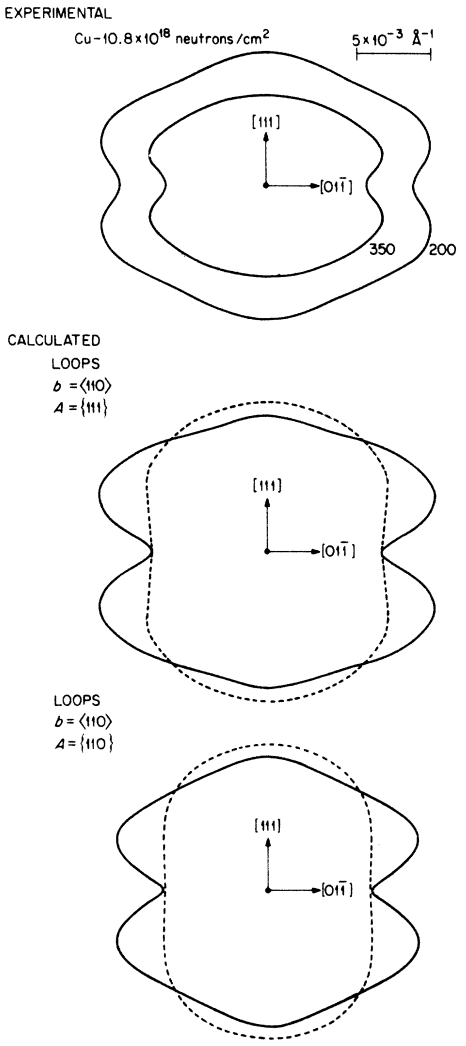

FIG. 7. Symmetric part of the diffuse scattering near the (111) reflection from neutron-irradiated copper. The calculations are for loops with Burgers vectors $b = \langle 110 \rangle$ on $\{111\}$ and $\{110\}$ planes assuming elastic isotropy (dashed) and anisotropy (solid) in the copper lattice.

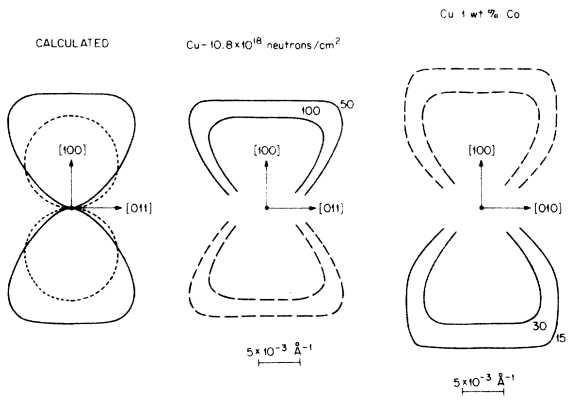

FIG. 8. Antisymmetrical diffuse scattering near the (200) reflection from Cu:1-wt%-Co and neutron-irradiated copper where the coarse dashed lines represent negative values in the measured curves. The calculated curves were obtained assuming elastic isotropy (dashed) and anisotropy (solid) in the copper lattice.

are qualitatively similar to those shown in Fig. 5 and with poorer resolution these two cases may not be distinguishable.

The antisymmetrical intensities, given by $\frac{1}{2}[I(\vec{q}) - I(-\vec{q})]$, are represented in Figs. 8 and 9. As mentioned in connection with Eq. (15), these contours should be nearly independent of the defect shape and except for the change in sign should have the same shape as that for spherical defects. The shape of the contours for the (200) case shows this directly, and even though the shape appears to be somewhat distorted from the calculated contours in the (111) case shown in Fig. 9, the antisymmetric contours are observed to be independent of the defect symmetry for this reflection also. The sign of the antisymmetric intensities for both reflections are in accord with the fact that the cobalt precipitates contract the host copper lattice in the Cu:1-wt%-Co crystal and the interstitial loops in the irradiated crystal expand the lattice. Since this intensity is obtained from the differences in the intensities for positive and negative $\vec{q}$'s, it has an inherently larger statistical error than the symmetric intensity and small deviations from the expected shape are therefore not considered serious at this point. The apparent reduction of intensity along the [111] direction in Fig. 9 may be due to an earlier falloff of $L_h(\vec{q})$ for this direction compared to the other directions. The relative intensities labeled on the contours in these figures are not necessarily scaled properly for comparison from one reflection or one sample to the other, but the symmetric and antisymmetric intensities are scaled properly with respect to their respective total intensities in Figs. 2 and 3.

Due to the influence of the resolution for the smaller $\vec{q}$ values and the proximity of the larger $\vec{q}$'s to the expected cutoff of the Huang scattering ($\sim 1.5 \times 10^{-2}$ Å for these samples), the $|\vec{q}|$ dependence cannot be considered in detail here, but will be studied with higher resolution measurements later. It should be pointed out, however, that even though some of the contours apparently extended beyond the Huang cutoff and at times continued in further than good resolution would allow, relatively little distortion was observed in the general shape of the contours. Therefore, considering the distribution of sizes of defects in these samples, it is felt that the measured contour shapes are reliable even though the $1/q^2$ and $1/q$ dependences of

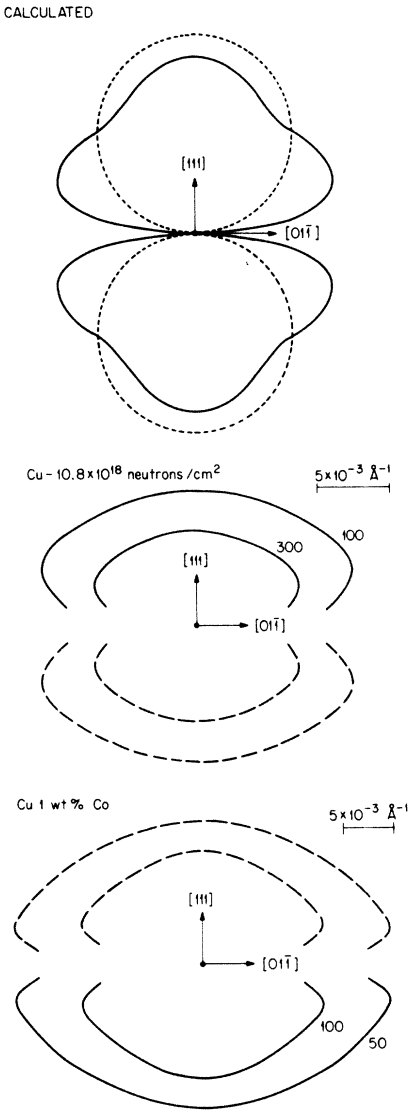

FIG. 9. Antisymmetrical diffuse scattering near the (111) reflection of Cu:1-wt%-Co and neutron-irradiated copper where the coarse dashed lines represent negative values in the measured curves. The calculated curves were obtained assuming elastic isotropy (dashed) and anisotropy (solid) in the copper lattice.

the symmetric and antisymmetric intensities, respectively, were not observable over the entire range of measurements. The generally good agreement with the calculated contours seems to bear this out also.

CONCLUSIONS

The Huang diffuse scattering resulting from the lattice distortions around dislocation loops in irradiated copper and cobalt precipitates in Cu:1-wt%-Co has been measured using a three-axis diffractometer. The resolution was sufficient to measure intensity contours around the (200) and (111) reflections and for separation into symmetric and antisymmetric components. The sign of the antisymmetric term showed that there were positive distortions around the dislocation loops and negative (inward) distortions around the cobalt precipitates. The shapes of the symmetric intensity contours were found to be in generally good agreement with those calculated using the dipole-force model for dislocation loops and spherical clusters when the elastic anisotropy of the copper lattice was considered. Contours calculated using an isotropic average set of elastic constants failed to represent the measured data. The contours of the antisymmetric scattering were found to be independent of the defect symmetry and dependent only on $\hat{h}$, as expected from the average over all cubic-equivalent defect orientations. The characteristic shapes of the contours were found to persist with little apparent distortion even into regions where $qR < 1$ was not strictly satisfied.

All of the expected symmetry aspects of the Huang diffuse scattering from dislocation loops and spherical clusters were observed for the (200) and (111) reflections, and the possibility of catagorizing defects as planar or spherical in nature was demonstrated. Additional detailed information, such as small deviations from sphericity or Burgers vector determination, was not derived from these measurements because such definite information would seem to require measurements with better vertical resolution in the region $qR \ll 1$. Such measurements can be limited to a few appropriate $\vec{q}$ directions rather than covering an entire plane since π_1, π_2, and π_3 are the only independent parameters of P_{nm} measurable by Huang scattering, as indicated by Eq. (9).

ACKNOWLEDGMENTS

The authors would like to thank F. W. Young, Jr. and T. S. Noggle for their help in providing crystals for this study and for discussions during this study.

*Research sponsored by the U. S. Atomic Energy Commission under contract with Union Carbide Corporation.
†Guest Scientist from Institut für Festkörperforschung der Kernforschungsanlage, Jülich, Germany.

[1]P. H. Dederichs, Phys. Rev. B 4, 1041 (1971).
[2]H. Trinkaus, Phys. Status Solidi B 51, 307 (1972).
[3]H. Trinkaus, Phys. Status Solidi B 54, 209 (1972).
[4]P. H. Dederichs, J. Phys. F 3, 471 (1973).

[5]P. Ehrhart and W. Schilling, Phys. Rev. B 8, 2604 (1973).
[6]H. Peisl (private communication).
[7]H. Spalt, H. Lohstöter, and H. Peisl, Phys. Status Solidi B 56, 469 (1973).
[8]P. Wombacher (unpublished).
[9]Bennett C. Larson and W. Schmatz (unpublished).
[10]M. A. Krivoglas, *Theory of X-Ray and Thermal Neutron Scattering by Real Crystals* (Plenum, New York, 1969).
[11]J. W. Flocken and J. R. Hardy, Phys. Rev. B 1, 2472 (1972).
[12]H. Kanzaki, J. Phys. Chem. Solids 2, 107 (1957).
[13]*International Tables for X-Ray Crystallography*, edited by K. Lonsdale (Kynoch, Birmingham, 1962), p. 233.
[14]P. Eisenberger, N. G. Alexandropoulos, and P. M. Platzman, Phys. Rev. Lett. 28, 1519 (1972).
[15]B. C. Larson and F. W. Young, Jr., Phys. Rev. B 4, 1709 (1971).
[16]Bennett C. Larson and F. W. Young, Jr., Z. Naturforsch. B 28, 626 (1973).
[17]Bennett C. Larson, J. Appl. Phys. 45, 514 (1974).
[18]W. Schmatz and Bennett C. Larson (unpublished).
[19]H. P. Degischer, Philos. Mag. 26, 1137 (1972).